PCCP

PAPER

View Article Online
View Journal | View Issue

Check for updates

Cite this: *Phys. Chem. Chem. Phys.*, 2018, **20**, 21417

Quantifying structure dependent responses in Li-ion cells with excess Li spinel cathodes: matching voltage and entropy profiles through mean field models†

Steffen Schlueter,[a] Ronny Genieser,[b] Daniel Richards,[c] Harry E. Hoster[ade] and Michael P. Mercer *[ade]

Measurements of the open circuit voltage of Li-ion cells have been extensively used as a non-destructive characterisation tool. Another technique based on entropy change measurements has also been applied for this purpose. More recently, both techniques have been used to make qualitative statements about aging in Li-ion cells. One proposed cause of cell failure is point defect formation in the electrode materials. The steps in voltage profiles, and the peaks in entropy profiles are sensitive to order/disorder transitions arising from Li/vacancy configurations, which are affected by the host lattice structures. We compare the entropy change results, voltage profiles and incremental capacity (dQ/dV) obtained from coin cells with spinel lithium manganese oxide (LMO) cathodes, $Li_{1+y}Mn_{2-y}O_4$, where excess Li y was added in the range $0 \leq y \leq 0.2$. A clear trend of entropy and dQ/dV peak amplitude decrease with excess Li amount was determined. The effect arises, in part, from the presence of pinned Li sites, which disturb the formation of the ordered phase. We modelled the voltage, dQ/dV and entropy results as a function of the interaction parameters and the excess Li amount, using a mean field approach. For a given pinning population, we demonstrated that the asymmetries observed in the dQ/dV peaks can be modelled by a single linear correction term. To replicate the observed peak separations, widths and magnitudes, we had to account for variation in the energy interaction parameters as a function of the excess Li amount, y. All Li–Li repulsion parameters in the model increased in value as the defect fraction, y, increased. Our paper shows how far a computational mean field approximation can replicate experimentally observed voltage, incremental capacity and entropy profiles in the presence of phase transitions.

Received 10th May 2018,
Accepted 25th July 2018

DOI: 10.1039/c8cp02989j

rsc.li/pccp

Open Access Article. Published on 25 July 2018. Downloaded on 6/18/2025 4:30:21 AM.
This article is licensed under a Creative Commons Attribution 3.0 Unported Licence.

1 Introduction

The growing demand for rechargeable batteries in electric vehicles and for stationary storage not only requires higher energy and power density, but also improved durability and safety.[1–5] One source of performance fade or failure in Li-ion cells is structural change in the electrode materials during cell operation.[6] A range of *in situ* methods have been developed and many of these have been applied to diagnose real-time changes in electrode structure from either thermal (calendar) aging or during prolonged charge/discharge cycling.[7–10] Additionally, there is a need for rapid validation of the electrochemical characteristics and quality of Li-ion cells from different suppliers. Improved quantification, ideally at the level of atomistic structure–property relationships, is needed to interpret existing *in situ* characterisation tools.

One class of promising techniques is based on thermodynamic measurements, a particular example of which is entropy profiling (EP).[10–28] This technique is based on the principle that the partial molar entropy change is proportional to the temperature response of the open circuit voltage (OCV) of a cell, by

$$\Delta S(x) = -nF\left(\frac{\partial E_{\mathrm{OCV}}(x)}{\partial T}\right)_{x,p}, \quad (1)$$

[a] *Department of Chemistry, Lancaster University, Bailrigg, Lancaster, LA1 4YB, UK. E-mail: m.mercer1@lancaster.ac.uk*
[b] *WMG Electrochemical Engineering Group, University of Warwick, Coventry, CV4 7AL, UK*
[c] *Imagination Lancaster, Lancaster University, Bailrigg, Lancaster, LA1 4YW, UK*
[d] *ALISTORE European Research Institute CNRS FR 3104, Hub de l'Energie, Rue Baudelocque, 80039 Amiens, France*
[e] *The Faraday Institution, Quad One, Harwell Science and Innovation Campus, Didcot, OX11 0RA, UK*

† Electronic supplementary information (ESI) available. See DOI: 10.1039/c8cp02989j

Open Access Article. Published on 25 July 2018. Downloaded on 6/18/2025 4:30:21 AM.
This article is licensed under a Creative Commons Attribution 3.0 Unported Licence.

where E_{OCV} is the open circuit voltage, T is the absolute temperature, p is the pressure, x is the fraction of Li intercalated in the electrode ($0 \leq x \leq 1$), n is the number of electrons transferred per extractable Li atom in the anode or cathode, F is the Faraday constant and the S is the entropy per mole of extractable Li.[17] These profiles are sensitive to order/disorder transitions in the Li/vacancy structure.[16,21,24,29]

Thompson *et al.* performed the first EP study on Li_xTiS_2 electrodes.[12] Selman *et al.* performed electrochemical-calorimetric measurements on $Li_xMn_2O_4$[13] and commercial Li-ion cells.[14] Reynier *et al.* investigated the entropy change upon intercalation into graphite and disordered carbons.[15,16] The entropy change during Li intercalation in graphite was recently investigated theoretically by Leiva *et al.*[30–32] Later work also investigated the entropy change in cathode materials, including Li_xCoO_2,[10,17–19] $Li_{x+y}Mn_{2-y}O_4$ spinel,[20–23] where y represents an excess amount of Li substituted in the 16d octahedral sites, $Li_xM_yMn_{2-y}O_4$,[20,24,25] where M denotes a metal defect, nickel manganese cobalt (NMC) based layered materials[26] and olivine Li_xFePO_4.[27,28] Furthermore, Maher *et al.*,[10,33] Osswald *et al.*[26] and Hudak *et al.*[18] examined the effect of prolonged charge/discharge cycles and calendar aging on the measured entropy profiles. They observed changes in the magnitudes of the peaks in profiles that were attributed to separate structural changes at the anode and cathode. A more comprehensive overview of entropy change measurements is available in a recent review by Zhang *et al.*[11]

Spinel lithium manganese oxide (LMO) electrodes are an attractive, low cost and non-toxic alternative to the many layered cathode structures currently used in commercial Li-ion cells. Entropy profiles of the stoichiometric compound, $Li_xMn_2O_4$ ($0 \leq x \leq 1$), show two well defined peaks. The peaks arise from the formation of an ordered phase, $Li_{0.5}Mn_2O_4$ at intermediate state of charge, and a transition to a disordered solid solution phase either side.[29,34–38] To better understand voltage and entropy profiles and enable more definitive structural assessments from them, we developed a Monte Carlo based model to quantify the changes in the EP peak amplitudes dependent on the proportion of point defects in $Li_xM_yMn_{2-y}O_4$ spinel (M = Co, Cr).[37] We showed that the experimental trends could be explained by pinned Li sites, required for charge balance, which occur in proportion to the defect fraction, y. More pinned Li sites imply that the ordered phase becomes progressively disrupted, resulting in a reduction in the EP and dQ/dV peak amplitudes.

To date, the information obtained from entropy profiling has been largely qualitative. Two approaches, which have already been applied to open circuit voltage (OCV) profiles[36,39–44] could be considered to also understand entropy profiles at a more quantitative level. On the one hand, *ab initio* approaches based on effective cluster interactions (ECIs) could be applied within a density functional theory (DFT) framework.[36,39,40] Although computationally complex and computer time intensive, these methods rely on minimal input parameters from experiments. On the other hand, parametric models can be directly fitted to experimental OCV profiles.[41–44] Although allowing rapid agreement between the models and experiment, the physical interpretation of the various parameters within the models, particularly the ones related to Li–Li interactions, is often unclear. Without an understanding of these parameters, it can be difficult to interpret the models when the cell chemistry is continuously changing, such as during cell aging.

The present work strives to gain an atomistic interpretation of OCV and entropy profiles while at the same time modelling experimental profiles with high throughput and accuracy. We focus on systematically varied cathode compositions, $Li_{1+y}Mn_{2-y}O_4$, in which a proportion, y, of Mn on the 16d sites is substituted by Li. To demonstrate the value of EP, we performed EP alongside standard voltage and dQ/dV characterisation, in coin cells with LMO cathodes prepared with excess Li values, y ($0 \leq y \leq 0.2$). This work sheds new light on the microscopic origins of the peaks observed in dQ/dV and EP, explaining how and why their amplitudes and positions change.

2 Methods

2.1 Synthesis of $Li_{1+y}Mn_{2-y}O_4$

All samples were prepared by a solid state reaction of $LiMn_2O_4$ (Alfa Aesar) and Li_2CO_3 (Sigma Aldrich). The $LiMn_2O_4$ powder was thoroughly mixed with the proportional amount of Li_2CO_3 in order to obtain the desired stoichiometry of $Li_{1+y}Mn_{2-y}O_4$. The mixture was heated up in a tube furnace to 600 °C for 18 h in air with a heating and cooling rate of 7 °C min^{-1}. Table 1 gives an overview of the synthesis conditions, the nominal amount of lithium from the synthesis and the lattice constants a of the samples, determined by X-ray diffraction (XRD) measurements.

Diffraction data was collected on a Rigaku Smartlab 9 kW using Cu Kα radiation (λ = 1.54 Å) over a 2θ range of 15–90° in Bragg–Brentano geometry with a step size of 0.01°. The lattice parameters were determined from the XRD pattern using the Rigaku PDXL 2, based on the crystal structure reported by Berg *et al.* (ICSD 50415).[45]

2.2 Electrochemical characterisation

For electrochemical testing, the different active materials were mixed with Super P (Alfa Aesar) as a conductive carbon and Solef PVDF (Solvay) as a binder in a ratio of 8 : 1 : 1. The resulting slurries, made with NMP (Sigma Aldrich), were coated on a 20 μm aluminium current collector and initially dried on a hot plate at 70 °C, then stored overnight at 50 °C under vacuum. Coin cells were assembled in a dry room using a Celgard 2325 separator, 150 μm Li foil (PI-KEM) and LP57 electrolyte: 1 M $LiPF_6$ in EC/DMC (3 : 7 vol%, BASF). A BaSyTec CTS cycler was used for the electrochemical and entropy characterisation.

Table 1 Synthesis conditions and lattice parameters of $Li_{1+y}Mn_{2-y}O_4$

Sample	Temperature (°C)	Excess Li, y	a (Å)
$Li_{1.00}Mn_{2.00}O_4$	—	0.00	8.2421(5)
$Li_{1.05}Mn_{1.95}O_4$	600	0.05	8.2319(0)
$Li_{1.10}Mn_{1.90}O_4$	600	0.10	8.2245(0)
$Li_{1.15}Mn_{1.85}O_4$	600	0.15	8.2144(0)
$Li_{1.20}Mn_{1.80}O_4$	600	0.20	8.2063(5)

Open Access Article. Published on 25 July 2018. Downloaded on 6/18/2025 4:30:21 AM.
This article is licensed under a Creative Commons Attribution 3.0 Unported Licence.

Two full galvanostatic cycles were performed on the half cells, each cycle comprising a galvanostatic charge starting from rest at 10 mA g^{-1} to a maximum voltage of 4.3 V *vs.* Li/Li^+. To ensure that the cell had reached its maximum state of charge, the cell was held at a constant voltage of 4.3 V for one hour. The cell was then galvanostatically discharged between 4.3 and 3.4 V at 10 mA g^{-1}, thus ending one cycle.

Voltage profiles were recorded at a high data acquisition rate of one data point per second. The dQ/dV curves were obtained firstly by numerical differentiation of the voltage curves from the second galvanostatic cycle, with charge and discharge being treated separately. The curves were then smoothed over 200 data points.

2.3 Entropy measurements

A custom made direct cooling and heating setup was used to change the temperature of the coin cells. The system consisted of an aluminum heat exchanger, in direct thermal contact with the coin cells, which is connected to a Julabo F12 refrigerated – heating circulator, allowing precise control over the temperature. The temperature was monitored by type-J thermocouples connected in multiple positions to the aluminium heat exchangers, which verified that temperature variation across the exchanger was negligible. For high resolution voltage and temperature acquisition a Keysight 34970A data logger was used. Entropy profiles were performed after fully charging the cells at 10 mA g^{-1} (with respect to the active mass of cathode material) to 4.3 V followed by a constant voltage step at 4.3 V for 2 hours.

To ensure all entropy measurements gave information comparable to the charge/discharge cycles, entropy measurements were performed immediately after two charge/discharge cycles as described in Section 2.2. After the second discharge, the cell was charged up to 4.4 V and held at constant voltage for two hours. This constant voltage step ensured that the cell was at maximum state of charge prior to commencing entropy profiling. To perform a full entropy profile, the cells were discharged stepwise with a current rate of 10 mA g^{-1} for 15 min, followed by voltage relaxation under open circuit (OC) conditions for 15 min. Both steps were performed at a temperature of 20 °C. Remaining under OC conditions, the temperature was then changed in 3 °C steps from 20 to 14 °C, each with a relaxation time of 15 min. Each iteration, shown in Table 2, was repeated 50 times or until the cell voltage was less than 3.8 V. To minimize the possible effects of self-discharge and to ensure that these rapid measurements were accurate we used our previously developed open circuit voltage (OCV) fitting and drift subtraction algorithms, described in detail by Osswald *et al.*[26]

Table 2 Experimental parameters of the entropy measurements

Step	Time (min)	Temperature (°C)
Discharge (10 mA h g^{-1})	15	20
Voltage relaxation (OC)	15	20
Temperature step 1 (OC)	15	17
Temperature step 2 (OC)	15	14
Temperature step 3 (OC)	15	20
Total time per step	75	

The variable of interest, ΔS_{conf}, the configurational entropy of Li/vacancy arrangements is measured by EP. However, there are also vibrational and electronic contributions, ΔS_{vib} and ΔS_{elec}, from the Li metal anode and the cathode,[17] so that the total ΔS obtained through EP is

$$\Delta S = \Delta S_{conf} + \Delta S_{vib} + \Delta S_{elec}. \quad (2)$$

The metallic Li anode can be considered as an infinite Li reservoir, with no lattice rearrangements possible during (de)intercalation. Hence, it can be considered to have a configurational entropy of zero[17] and is expected to contribute negligibly to the entropy profiles compared with the configurational entropy change of the cathode. In the entropy profiles of Li_xCoO_2, ΔS_{elec} was shown to be negligible and this is likely to be true for all semiconducting transition metal oxides.[17] According to Fultz *et al.*[17] ΔS_{vib} can be treated as a constant background contribution across the intercalation range. We adopted this approximation in our numerical optimisation procedures, as described in Section 2.5.

2.4 Statistical mechanical model

Our modelling approach is based on the one adopted by Leiva *et al.* who applied the model to graphite.[31,32] The calculations were performed within the canonical ensemble, under the Bragg–Williams approximation.

For the spinel lattice $Li_xMn_2O_4$, $(0 \leq x \leq 1)$, the Li atoms adopt a diamond lattice structure, which can be reduced to two laterally separated face centred cubic sublattices, as shown previously.[29,34,46] We considered a lattice of $2M$ sites, where M is the number of sites on each sublattice. A total of $M = 100$ was found to be fully converged with respect to the system size and this value was used in all simulations. Given two fractional sublattice occupancies n_1 and n_2, such that $0 \leq n_1, n_2 \leq 1$, the overall fraction of Li on the 8a sites, x, is given by

$$x = \frac{(n_1 + n_2)}{2}. \quad (3)$$

The total number of occupied sites, N, is $N = 2Mx$. The assumption of the Bragg–Williams approximation is that all Li/vacancy configurations for a particular set of values n_1 and n_2 are degenerate, where the number of degenerate energy levels is Ω_j for a state j. In practice, for a given x value, the calculation is performed by enumerating through all possible values of n_1 and n_2, assuming the energy expression is not affected by the local arrangement of Li atoms. Under the assumption that the different configurations for fixed n_1 and n_2 are degenerate, we can write the Hamiltonian, $H(N,M)$ which describes the energy of the entire system, as

$$H(N,M) = \langle \varepsilon_1 \rangle \langle N_1 \rangle + \langle \varepsilon_2 \rangle \langle N_2 \rangle, \quad (4)$$

where $\langle N_1 \rangle = \langle n_1 \rangle M$ and $\langle N_2 \rangle = \langle n_2 \rangle M$ are the total number of atoms on sublattices 1 and 2 respectively, and the brackets here denote averaged quantities. We used a pairwise interaction model for the spinel lattice, similar to the one adopted elsewhere.[29,34,37,46] In the filled lattice, $x = 1$, each Li atom has $N_{nn} = 4$ nearest neighbours on opposite sublattices and $N_{nnn} = 12$ next nearest

Open Access Article. Published on 25 July 2018. Downloaded on 6/18/2025 4:30:21 AM.
This article is licensed under a Creative Commons Attribution 3.0 Unported Licence.

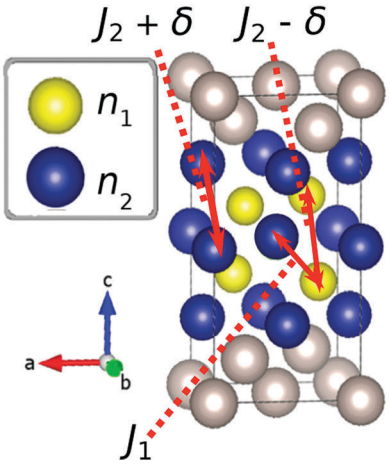

Fig. 1 Representation of the diamond lattice structure, adopted by the Li atoms in spinel $LiMn_2O_4$. Here a (1 × 1 × 2) unit cell is shown. The interaction terms J_1, J_2 and δ are described in the main text.

neighbours on like sublattices. The pairwise interaction model is shown in Fig. 1.

$\langle\varepsilon_1\rangle$ and $\langle\varepsilon_2\rangle$, the average energies per site associated with each of the sublattices, are given by

$$\langle\varepsilon_1\rangle = -\varepsilon_0 + \frac{1}{2}J_1 N_{\mathrm{nn}}\langle n_2\rangle + \frac{1}{2}(J_2+\delta)N_{\mathrm{nnn}}\langle n_1\rangle, \quad (5)$$

$$\langle\varepsilon_2\rangle = -\varepsilon_0 + \frac{1}{2}J_1 N_{\mathrm{nn}}\langle n_1\rangle + \frac{1}{2}(J_2-\delta)N_{\mathrm{nnn}}\langle n_2\rangle, \quad (6)$$

where ε_0 is the point term for Li–lattice interactions, J_1 and J_2 are the nearest and second nearest neighbour interaction parameters, respectively and δ is an energy separation between the J_2 parameters on each of the sublattices. The prefactors of 1/2 have to be included on both pairwise interaction terms to avoid double counting each pair.

We can define the partition function, as shown by Leiva *et al.*[31]

$$Q(N,2M) = \sum_i \mathrm{e}^{-\frac{E_i}{k_\mathrm{B}T}} = \sum_{j=0}^{N}\Omega_j \mathrm{e}^{-\frac{E_j}{k_\mathrm{B}T}}, \quad (7)$$

where the index i indicates summation over all possible Li/vacancy configurations while index j indicates summation over degenerate energy levels, E_j, where the degeneracy is given by Ω_j. Our own code, written in Python 2.7.12, was run on a conventional PC, exploiting the summation over j to reduce the computational burden.

Ω_j can be determined as using the expressions shown elsewhere,[31] *i.e.* for $N < M$

$$\Omega_j = \frac{(M!)^2}{(M-N+j)!(N-j)!(M-j)j!}, \quad (8)$$

otherwise

$$\Omega_j = \frac{(M!)^2}{(2M-N-j)!(N-M+j)!(M-j)j!}. \quad (9)$$

We used the Stirling approximation, $\ln(k!) \approx \ln\left(\left(\frac{k}{e}\right)^k\right) = k(\ln(k)-1)$ on the terms Ω_j.

As for the energy terms, E_j, these can be determined by

$$E_j = \begin{cases} (N-j)\varepsilon_1 + j\varepsilon_2 & \text{for } N < M \\ (M-j)\varepsilon_1 + (N-M+j)\varepsilon_2 & \text{for } N \geq M \end{cases}. \quad (10)$$

We can write modified forms of eqn (5) and (6), but now in terms of the index, j

$$\varepsilon_1 = -\varepsilon_0 + 2J_1 n_2 + 6(J_2+\delta)n_1, \quad (11)$$

$$\varepsilon_2 = -\varepsilon_0 + 2J_1 n_1 + 6(J_2-\delta)n_2, \quad (12)$$

where the terms ε_1 and ε_2 describe the energies per site of sublattice 1 and 2, respectively, dependent on j. The sublattice occupancies n_1 and n_2 in eqn (11) and (12) are explicitly determined by the index j while performing the summation in eqn (7), *i.e.* for $N < M$, $n_1 = (N-j)/N$ and $n_2 = j/N$. Similar expressions for these occupancies can be determined by inspection of eqn (10) when $N \geq M$.

From the partition function, eqn (7), the chemical potential, μ, can be determined as

$$\mu = -k_\mathrm{B}T\left(\frac{\partial \ln Q}{\partial N}\right)_{T,M}, \quad (13)$$

and we used similar thermodynamic expressions, shown elsewhere,[31] to evaluate the partial molar entropy. From the relationship $V = -e/\mu$, where V is the voltage *versus* a metallic Li anode,[47] all simulated voltage profiles were determined.

Eqn (5) and (6) are very similar to the ones applied previously to $Li_xMn_2O_4$ and graphite. A new development is the introduction of the term δ. This was motivated by previous experimental dQ/dV studies,[34,48] along with our own results, which indicated two different peak amplitudes for $Li_xMn_2O_4$. With pairwise interactions, this asymmetry cannot be explained with the usual assumption of $\delta = 0$, because in this instance the interactions are symmetric with respect to particles and vacancies.

To describe the effect of excess Li in $Li_{x+y}Mn_{2-y}O_4$, where y is the amount of Li placed on the 16d sites, we assumed a total of $3y$ 8a sites were pinned to the lattice in random positions, as proposed and modelled by Gao *et al.*[34] The Li occupations on the 8a sites can then be expressed as

$$n_1 = z_1(1-3y) + 3y, \quad (14)$$

$$n_2 = z_2(1-3y) + 3y, \quad (15)$$

where $0 < z_1, z_2 < 1$ are the fractional occupations of removable Li on the remaining unpinned 8a sites. Then all other thermodynamic variables were determined as for the specific case $y = 0$, except that the degeneracy, Ω_j, was evaluated over a reduced number of sites, $M' = M(1-3y)$. We assumed *a priori* that the interactions from these sites were unaffected by excess Li, hence the totals N_1 and N_2 in eqn (4) included all 8a Li sites.

2.5 Numerical optimisation

To fit experimental and simulated data, the Nelder–Mead simplex optimisation method was used.[49] This was implemented using the "minimize" function from the Scipy library of Python. In particular, to ensure reliability of the parameters, dQ/dV and

Open Access Article. Published on 25 July 2018. Downloaded on 6/18/2025 4:30:21 AM.
This article is licensed under a Creative Commons Attribution 3.0 Unported Licence.

entropy profiles were fitted simultaneously, so that the overall objective function of the minimization, $f(\theta)$, was given by

$$f(\theta) = 4 \arg\min_{\theta} f_{Q'}(\theta) + \arg\min_{\theta} f_{S'}(\theta), \quad (16)$$

where

$$\arg\min_{\theta} f_{Q'}(\theta) = \sqrt{\frac{\sum_{i=1}^{2M} \left(\hat{Q}_i'(\theta) - Q_i'\right)^2}{2M}}, \quad (17)$$

and

$$\arg\min_{\theta} f_{S'}(\theta) = \sqrt{\frac{\sum_{i=1}^{2M} \left(\hat{S}_i'(\theta) - S_i'\right)^2}{2M}}, \quad (18)$$

where $f_{Q'}(\theta)$ and $f_{S'}(\theta)$, are the respective objective functions for dS/dx and dQ/dV respectively, Q_i', S_i' refer to the experimental dQ/dV and dS/dx results, $\hat{Q}_i'(\theta)$ and $\hat{S}_i'(\theta)$ are the corresponding simulated data and θ, the arguments of the minimisation, were given by

$$\theta = [\varepsilon_0 J_1 J_2 \delta \Delta S_{vib}] \quad (19)$$

where all variables, apart from ΔS_{vib}, were defined in Section 2.4. As for ΔS_{vib}, it is a correction term to the entropy profiles arising predominantly from vibrational contributions to the entropy.[17] Based on the inelastic neutron scattering experiments of Fultz *et al.*,[17] it was treated a constant vertical correction to the dS/dx profiles; it was assumed to have no effect on dQ/dV. The experimental data points were interpolated onto the range of points from the simulated data using the ''interp1d'' function from the Scipy library. Cubic spline interpolation was chosen. The weighting factor of 4 in eqn (16) was determined by independent fitting of Q' and S'. For all 5 excess Li values tested, it was found that the value of the objective function in S' (eqn (18)) was approximately 4 times that of Q' (eqn (17)). For convenience, we use the shorthand notation $4Q'$ and S' for the quantities in eqn (17) and (18), respectively.

To ensure reliability of the optimisation method it was found to be critical to determine a suitable initial trial value for the simplex optimisation. This was achieved by starting with a brute force grid search. The grid was a 5-dimensional array with uniformly spaced points, whose limits were successively reduced in size between successive grids. This was achieved by determining the value of $f(\theta)$ from the previous grid, and using the input arguments θ to determine the limits of the new grid. The starting values of the simplex search are specified in Table 3, where θ^0_{min}, θ^0_{max}, θ^0_{int} were the maximum value, minimum value, and grid interval for each respective parameter of iteration 1, respectively. The grid was dynamically updated, using the optimal solution from the previous search to determine the next grid. The corresponding values of θ^i_{min}, θ^i_{max}, θ^i_{int} (first iteration $i = 0$) were determined by

$$\theta^i_{min} = (f(\theta)_{i-1} + \theta^{i-1}_{min})/2 \quad (20)$$

$$\theta^i_{max} = (f(\theta)_{i-1} + \theta^{i-1}_{max})/2 \quad (21)$$

Table 3 Values used to initialise the grid search

θ	θ^0_{min}	θ^0_{max}	θ^0_{int}
ε_0	4.090	4.350	0.032
J_1	25.0	75.0	5.0
J_2	−2.0	17.0	1.5
δ	1.0	8.0	1.0
ΔS_{vib}	−10.0	−2.0	2.0

$$\theta^i_{int} = (\theta^i_{max} - \theta^i_{min})/6 \quad (22)$$

where i denotes the number of the iteration and $f(\theta)_{i-1}$ denotes the optimal function value determined from the previous iteration.

6 successive grids were applied (up to and including $i = 5$) and the arguments θ corresponding to the smallest objective value obtained from all 6 grids was used to initialise the simplex search. It was found that this procedure was the only way to guarantee reliable fitting when the excess Li content, y, was greater than 0.10.

To avoid a fitting bias towards the end points of the state of charge, for both $f_{Q'}(\theta)$ and $f_{S'}(\theta)$ the fit was constrained to data points in the range 3.95 V $\leq V \leq$ 4.15 V, where V is the voltage. Output from the fitting process is presented in the ESI,† Fig. S1.

3 Results

3.1 X-ray diffraction

The XRD pattern of $Li_{1+y}Mn_{2-y}O_4$ with different values of y are shown in Fig. 2a. On the right hand side, the (111) peak is highlighted over a narrower Bragg angle range. With higher lithium content the reflections shift to higher 2θ values compared to those of stoichiometric $LiMn_2O_4$. The enlarged XRD pattern highlights this shift and as result the lattice parameters of the $Fd\bar{3}m$ unit cell decrease with increasing excess Li. The decrease of the lattice parameter a follows an approximately linear relationship with the nominal amount y in $Li_{1+y}Mn_{2-y}O_4$ in the investigated range (Fig. 2b), in good agreement with reported results.[50,51] The theoretical average oxidation state of manganese increases from 3.50 ($y = 0$) to 3.78 ($y = 0.20$), also shown in Table 4, *i.e.* the proportion of Mn^{3+} decreases with y. The ionic radii of Mn^{3+} and of Mn^{4+} are, respectively, 0.65 Å and 0.53 Å.[52] By substituting Mn^{3+} with Li^+ ions the proportion of the larger Mn^{3+} ions decreases, resulting in a concomitant decrease in unit cell size.

3.2 Voltage profiles

For completeness and to ensure the validity of our results, we show voltage profiling results over a range of compositions, which are in line with those already published.[2,53] The stoichiometric compound, defect concentration $y = 0$ has poor capacity retention between the first charge and first discharge cycles, as shown here and elsewhere.[34,54–56] For these reasons, it is not used in this form in the cathode materials of commercial cells, but requires defect substitution, such as the intentional introduction of excess Li. Therefore, the materials with excess Li substituted, in the range $0.05 \leq y \leq 0.2$ (y = excess Li fraction), are more representative of the materials actually used in

Open Access Article. Published on 25 July 2018. Downloaded on 6/18/2025 4:30:21 AM.
This article is licensed under a Creative Commons Attribution 3.0 Unported Licence.

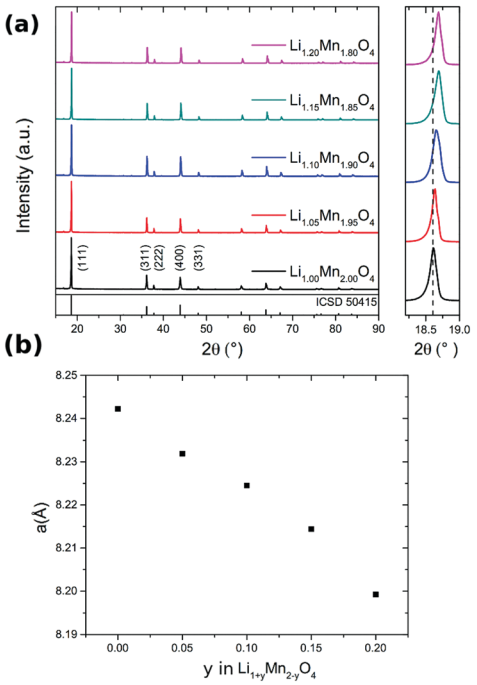

Fig. 2 (a) XRD pattern of $Li_{1+y}Mn_{2-y}O_4$ ($0 \leq y \leq 0.2$). The enlarged diffraction pattern on the right side highlights the shift of the (111) peak, indicating a decrease in lattice parameter *a* as a function of *y*. (b) Variation of *a* as a function of the excess lithium content, *y*.

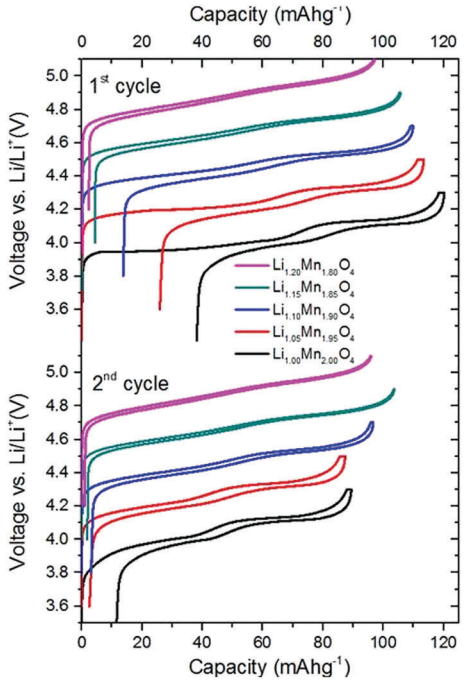

Fig. 3 First and second charge and discharge cycles of $Li_{1+y}Mn_{2-y}O_4$ ($0 \leq y \leq 0.2$) between 3.4 V and 4.3 V at 20 °C. Charge and discharge were performed at a current rate of 10 mA g^{-1}. Please note: for clarity, the curves are each vertically offset by 0.2 V. The true voltage range is shown by the black curves, *i.e.* the curves corresponding to $LiMn_2O_4$.

commercial Li-ion cells.[2,53] Our primary aim is not to assess the trends in the discharge capacity or Coulombic efficiency of these compounds as a function of the composition. Rather, we show how shape changes in the voltage profiles themselves can be related to changes in the underlying excess Li (point defect) concentration in the electrode materials. We show results over the entire compositional range $0 \leq y \leq 0.2$ to provide the maximum number of data points to validate our model and clearly identify the trends in the changes in shape of the curves.

The first and second charge/discharge profiles are shown in Fig. 3. Here, each full cycle denotes one charge followed by one discharge; no electrochemical treatment was performed prior to the first cycle. The capacity during the first charge decreases monotonically with increasing amount of excess lithium, *y*. The stoichiometric compound $LiMn_2O_4$ reaches a first cycle capacity (during charge) of 120 mA h g^{-1} whereas $Li_{1.2}Mn_{1.8}O_4$ only reaches 100 mA h g^{-1}.

The stoichiometric compound loses approximately 30 mA h g^{-1} in the first cycle, which is comparable to the capacity loss shown in another study of stoichiometric LMO.[54] The instability of this compound during electrochemical characterisation is well known.[34,54–56] Hao *et al.*[54] attributed the loss of capacity to particle cracking and a concomitant loss of active material. Alternative explanations that have been proposed are Mn disproportionation and structural distortions, such as the Jahn–Teller effect.[4,34,53–56] The absolute capacity loss between the first charge and discharge cycles varies systematically with *y*. As shown in Table 4, excess Li raises the average oxidation state (AOS) of Mn, reducing the fraction of Mn^{3+} and hence reducing capacity loss due to Mn disproportionation[6] and structural distortions.

The curves obtained during the second cycle are more representative of the performance of the cathode materials and hence these curves were used for further analysis of differences in shape in the voltage profiles as a function of the material composition. In stoichiometric $LiMn_2O_4$, a kink in the voltage profiles can be observed at around 4.05 V; as the amount of *y* increases the kink becomes progressively less visible. This feature has been attributed to an order/disorder transition in

Table 4 Theoretical average oxidation states (AOS) of $Li_{1+y}Mn_{2-y}O_4$. Occupancies of all the sites in the charged and discharged states are shown

Excess Li (*y*)	Discharged state	Mn AOS (discharged)	Mn AOS (charged)	Charged state assuming 3*y* pinning
0.00	$[Li_{1.00}]_{8a}[Li_{0.00}Mn_{2.00}]_{16d}O_4$	3.50	4.00	$[Li_{0.00}]_{8a}[Li_{0.00}Mn_{2.00}]_{16d}O_4$
0.05	$[Li_{1.00}]_{8a}[Li_{0.05}Mn_{1.95}]_{16d}O_4$	3.56	4.00	$[Li_{0.15}]_{8a}[Li_{0.05}Mn_{1.95}]_{16d}O_4$
0.10	$[Li_{1.00}]_{8a}[Li_{0.10}Mn_{1.90}]_{16d}O_4$	3.63	4.00	$[Li_{0.30}]_{8a}[Li_{0.10}Mn_{1.90}]_{16d}O_4$
0.15	$[Li_{1.00}]_{8a}[Li_{0.15}Mn_{1.85}]_{16d}O_4$	3.70	4.00	$[Li_{0.45}]_{8a}[Li_{0.15}Mn_{1.85}]_{16d}O_4$
0.20	$[Li_{1.00}]_{8a}[Li_{0.20}Mn_{1.80}]_{16d}O_4$	3.78	4.00	$[Li_{0.60}]_{8a}[Li_{0.20}Mn_{1.80}]_{16d}O_4$

This journal is © the Owner Societies 2018

Open Access Article. Published on 25 July 2018. Downloaded on 6/18/2025 4:30:21 AM.
This article is licensed under a Creative Commons Attribution 3.0 Unported Licence.

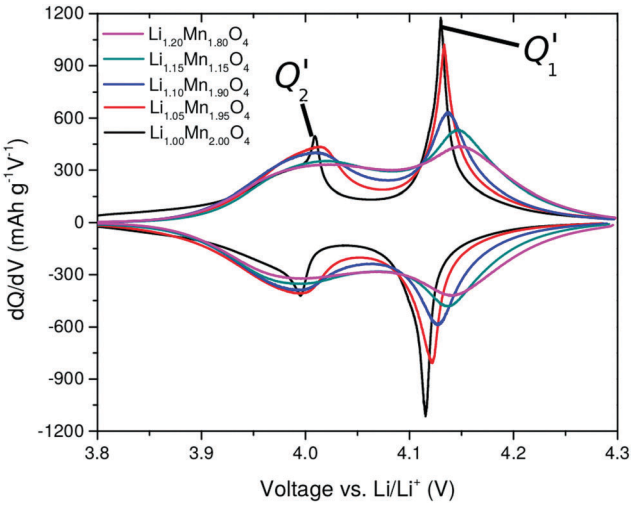

Fig. 4 Incremental capacity curves dQ/dV, obtained from the second cycle in Fig. 3. The two peaks, Q_1' and Q_2', are highlighted.

the Li/vacancy structure.[25,29,34,36,37,57] This effect is also visible in the incremental capacity (dQ/dV) curves shown in Fig. 4. The peak amplitudes at about 4 V and 4.15 V decrease with increasing 16d lithium content, y. We can attribute this effect to a suppression of the order/disorder transition, as shown previously by us[37] and others.[21,25,34] We and Gao *et al.*[50] proposed that the ordered phase, $Li_{0.5}Mn_2O_4$, is suppressed by pinned Li sites, as shown in Fig. 5.

Table 4 gives an overview of the theoretical average oxidation state (AOS) of the samples and highlights the occupied 8a Li sites in the charged and discharged states. It has been proposed that a proportion of Li, x_{pin} remains "pinned" on some of the 6 8a sites in the neighbourhood of each substituted 16d Li site.[34] To retain charge balance, the proportion of pinned Li sites would be $3y$.

A further observation is that the two peaks, Q_1' and Q_2' in dQ/dV (Fig. 4) are of unequal amplitudes, widths and shapes. This is true for all y values but the effect is more pronounced for low y. The issue previously been described but its origin is controversial; it could arise from the permselectivity effect during Li (de)insertion or from elastic contributions.[58–60] We propose that it is related changes in interactions in the system during Li (de)insertion as well as the effect of the pinned Li sites, as we show in Section 3.5. The dQ/dV profiles can be validated further through entropy profiling (Section 3.3) and modelling (Section 3.5). We can directly compare dQ/dV with the thermodynamic information obtainable through entropy profiling, as presented in the next section.

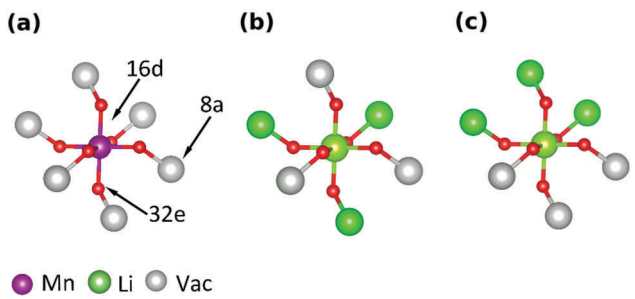

Fig. 5 Representations of the local environment around an octahedral 16d site, in the fully charged state. Oxygen 32e sites clearly show the octahedral coordination. The 6 nearest neighbour 8a sites to the shown 16d site are indicated. (a) Environment around a Mn site. All 8a Li sites are vacant. (b and c): Li substitutes for Mn on a 16d site, resulting in 3 nearest neighbour Li sites being pinned. (b and c) Represent two possible coordinations of the pinned Li sites.

3.3 Entropy profiles

Entropy profile results, as a function of the excess Li amount, y, are shown in Fig. 6. For $y = 0$, two peaks are observed in the profiles at about 4 V and 4.1 V. The results show a systematic decrease in the amplitude of the two peaks as y increases. These peaks, S_1' and S_2', occur due to a transition to an ordered phase, $Li_{0.5}Mn_2O_4$, close to $x = 0.5$, and a transition to a disordered solid solution region either side of $x = 0.5$.[29] Most previous work compared the entropy response of $LiMn_2O_4$ with one composition in which a proportion of Mn was substituted with Cr, Co, Al or Li.[21,24,25] Yazami *et al.* performed entropy profiling on $LiMn_2O_4$ and $Li_{1.08}Mn_{1.92}O_4$, but did not observe a significant change in entropy peak amplitude.[21] A clear and systematic trend is shown here for the first time over a range of excess Li compositions, indicating that excess Li systematically suppresses the order/disorder transition. The trend is in line with the experimental results of Kobayashi *et al.* for Cr and Co substitution[24,25] and previously modelled by us using Monte Carlo methods.[37]

Within the hypothesis that the reduction in the amplitudes of S_1' and S_2' arises from the pinned Li sites, two populations of Li in the 8a sites should be considered: the total 8a proportion, $3y \leq x \leq 1$, and only the fraction of removable Li, $0 \leq x_r \leq 1$. These populations are related by

$$x_r = \frac{x - 3y}{1 - 3y}. \quad (23)$$

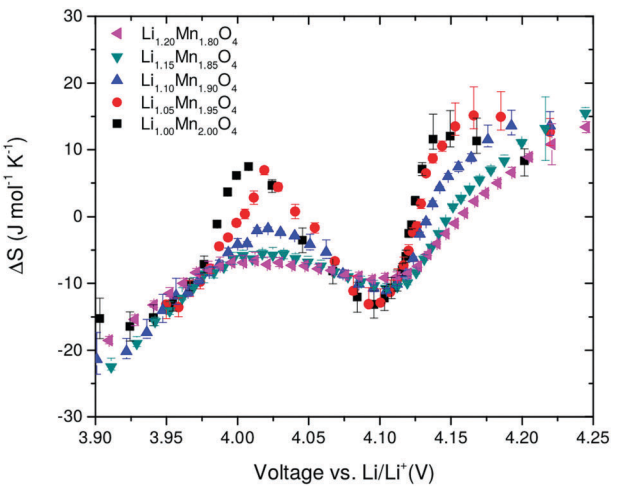

Fig. 6 Entropy change as a function of open circuit voltage (OCV) obtained after background subtraction. The amount of excess Li, y, is shown in the legend.

Open Access Article. Published on 25 July 2018. Downloaded on 6/18/2025 4:30:21 AM.
This article is licensed under a Creative Commons Attribution 3.0 Unported Licence.

In entropy profiling, only entropy changes arising from the removable Li population are probed, since in the approximation we have adopted here, the pinned sites adopt one fixed, immovable configuration over the experimentally measured voltage range. Thus

$$\Delta S = \frac{\mathrm{d}S}{\mathrm{d}x_\mathrm{r}}. \tag{24}$$

This is consistent with the fact that we defined ΔS per mole of removable Li in eqn (1), allowing entropy changes in the anode and cathode to be compared in a 1 : 1 fashion. We can gain further insight to interpret the entropy and voltage profile results through modelling, as shown in the subsequent section. This also allows us to compare profiles with respect to the two 8a Li populations, x_r and x.

3.4 Effect of parameter variation within the model

3.4.1 Effect of varying J_1. To understand the effect of the substitution of Li for Mn on the entropy and voltage profiles, a mean field lattice model based on the Bragg–Williams approximation was used, as explained in Section 2.4. The effect of changing the nearest neighbour lattice interaction parameter, J_1 is shown in Fig. 7 and 8.

The overall trend in peak amplitude is most clearly shown by plotting the profiles as a function of x, as in Fig. 8. Fig. 8c shows that with J_1 = 0 meV, the lithium ions are distributed with the same probability over all sites in the lattice, with a maximum in the entropy, at x = 0.5 as expected for an ideal solid solution. In the region $0.0 < J_1 < 25$ meV, the entropy maximum at x = 0.5 slowly decreases with J_1. At J_1 = 25 meV, incomplete peak separation results in a flat entropy maximum. The increase in lateral repulsions is also reflected in the voltage profiles, shown in Fig. 8a, which indicate a widening of the voltage window as a function of J_1. Increasing J_1 further causes the formation of two distinct entropy peaks, as shown Fig. 8c. The peak magnitudes increase with higher J_1. This is related to the formation of an ordered phase at x = 0.5, which is stable over an increasing voltage range as J_1 increases. The x values of the entropy maxima correspond very closely to the two maxima observed in dx/dV, as shown in Fig. 8b. These profiles, proportional to dQ/dV, show extra peaks compared with the entropy response,

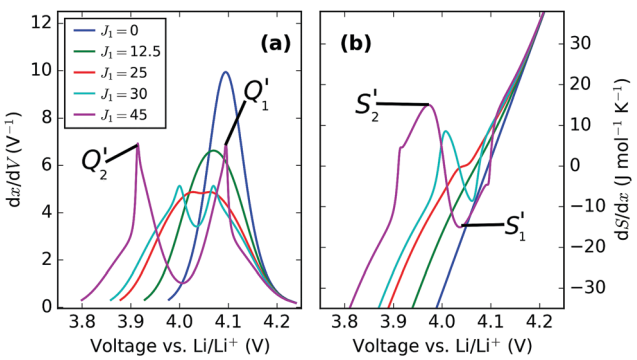

Fig. 7 dx/dV and dS/dx, shown here as a function of voltage. J_1 value, in meV, is shown in the legend, with ε_0 = 4.10 eV.

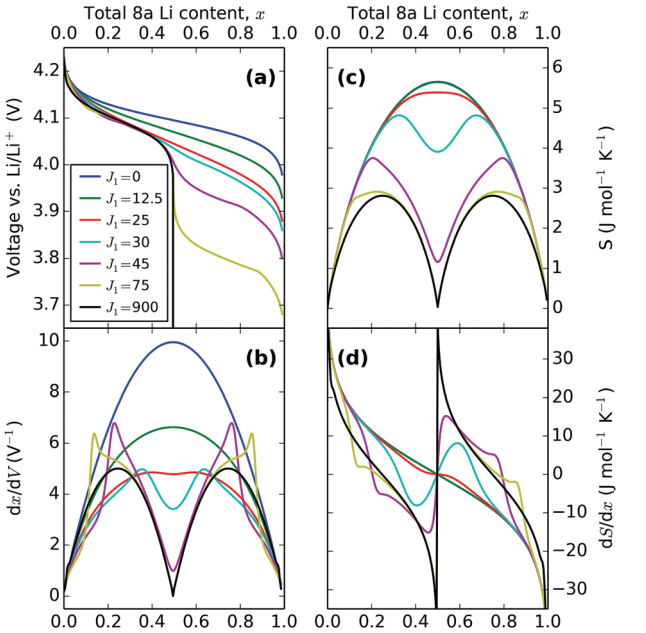

Fig. 8 Effect of varying J_1 with ε_0 = 4.10 eV. J_1 value, in meV, is shown in the legend.

because of the Li–Li interactions from the J_1 parameter. Eventually, at the most extreme values of J_1, the two sublattices are filled sequentially and can be treated as two independent solid solutions, resulting in a discontinuity in the partial molar entropy (black line in Fig. 8d). These results are in line with the ones of Otero *et al.* who applied a very similar statistical mechanical model to Li intercalation in graphite,[32] along with previous models of LMO.[29,34,46,58]

Trends in the peak variation with J_1, with respect to voltage, are shown in Fig. 7. Both profiles show the voltage window widening with increasing Li–Li repulsion, J_1, consistent with the voltage profiles in Fig. 8a. Consequently, the peak separations with respect to voltage in dx/dV and dS/dx increase even further with J_1 than in Fig. 8b and d, with the result that the experimentally obtained profile separations are extremely sensitive to the interaction parameters.

3.4.2 Effect of varying J_2. A comparison with the experimental results, Fig. 3, 4 and 6 suggests that repulsive J_1 on the order of 30 meV is required. To more accurately model the sharp peak in dx/dV, previous work introduced an attractive next nearest neighbour parameter, J_2.[29,34,46] We show the effect of attractive (negative) and repulsive (positive) J_2 with constant J_1 on the experimental observable profiles in Fig. 9.

The voltage profiles, Fig. 9a, show the trend in the change of voltage window with J_2 to be similar to that of J_1, *i.e.* the window widens with an increase in parameter value. However, the change in slope between about 3.95 and 4.10 V becomes more pronounced with attractive J_2, while repulsive J_2 suppresses it, *i.e.* both parameters have opposite effects on the order/disorder transition. The effect is even more clearly shown by the dx/dV and dS/dx profiles, Fig. 9b and c. Therefore, the two parameters have clearly distinguishable effects. In particular, the peak profile

 This journal is © the Owner Societies 2018

Open Access Article. Published on 25 July 2018. Downloaded on 6/18/2025 4:30:21 AM.
This article is licensed under a Creative Commons Attribution 3.0 Unported Licence.

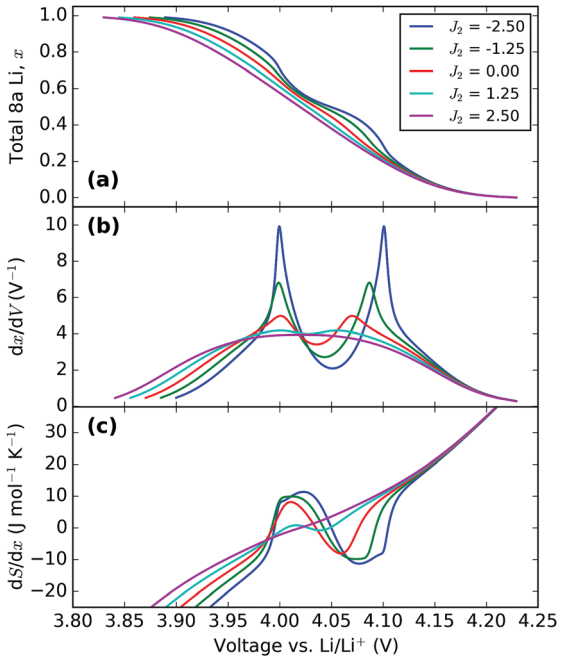

Fig. 9 Effect of varying the next nearest neighbour parameter, J_2. All profiles were obtained with J_1 = 30 meV and ε_0 = 4.10 eV. The value of J_2 (in meV) in each instance is indicated in the legend.

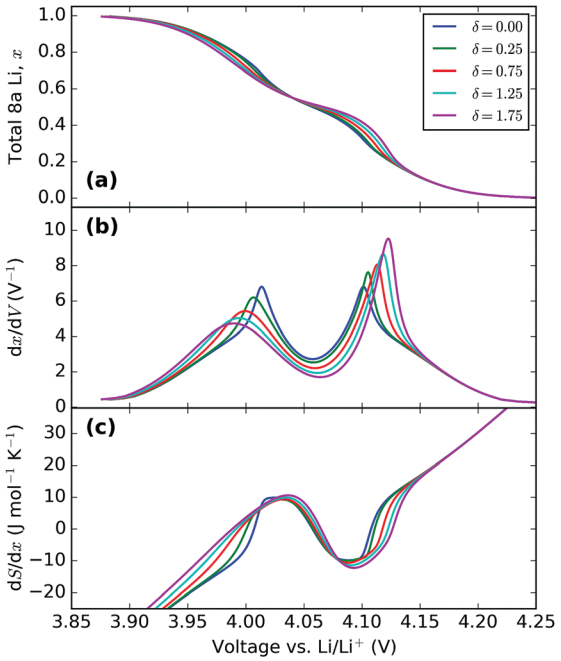

Fig. 10 Effect of varying the energy separation, δ. All profiles were obtained with ε_0 = 4.10 eV, J_1 = 30 meV and J_2 = −1.25 meV. The value of δ (in meV) in each instance is indicated in the legend.

separation increase with decreasing J_2 is much less marked than when J_1 is increased. Alternatively, for the same peak separation much greater amplitude changes can be obtained by varying J_2 rather than J_1.

3.4.3 Effect of varying δ. The result for dx/dV, Fig. 9b, suggests that to model the sharp peak, Q_1', observed for $Li_xMn_2O_4$, a small attractive interaction on the order of $J_2 = -1$ meV is required. However, regardless of the parameter values, the symmetry between Li and vacancies is always preserved, due to the symmetry of pairwise interactions. In contrast, Fig. 4, along with other studies of $Li_xMn_2O_4$,[34,48,61] show two peaks, Q_1' and Q_2', with distinct widths and amplitudes, indicating changes in the lattice during Li (de)insertion. To simulate the effect, we introduce a linear correction term δ, between the interaction J_2 on the most and least occupied sublattices, as shown in eqn (5) and (6). The results are shown in Fig. 10.

Increasing δ increases the peak amplitude difference between Q_1' and Q_2'. This reflects the actual changes seen in experiments, as shown in Fig. 4. The change in interaction parameter could be due to lattice expansion during intercalation as observed by Yang *et al.*[62] and Palacin *et al.*[63] using *in situ* XRD.

3.4.4 Effect of excess Li, y, with constant energy parameters. Results for variable Li excess, y, are presented, using the optimal interaction parameters determined for $y = 0$, $Li_xMn_2O_4$. Fig. 11a–c show results considering the total amount of Li in the structure, $3y \leq x \leq 1$. Results are plotted with respect to removable Li, $0 \leq x_r \leq 1$, in Fig. 11d–f.

The results in Fig. 11a and b are in general agreement with those of Gao *et al.*[34] The pinned Li sites cause a reduction in available capacity. Moreover, they result in a suppression of the order/disorder transition, also visible in the entropy profiles, Fig. 11c, as well as smaller dx/dV peaks, shown in Fig. 11b. For the first time we can also see that the peak amplitude difference resulting from the constant energy separation, δ = 1.25 meV, between the J_2 interaction parameter on each sublattice, is also suppressed with increasing y. These results are all in qualitative agreement with experiment, providing validation of the model.

Because the practical capacity of these electrodes changes during charge/discharge cycling, and there are uncertainties associated with determining the voltage limits at the two extremes of the solid solution region $x_r \to 0$ and $x_r \to 1$ it can be difficult to relate the vertical scales between models and experimental data. Showing the same results with respect to the removable Li population, as in Fig. 11d–f allows us to directly compare simulated and experimental curves.

In the simulated voltage profiles, Fig. 11d, the low voltage plateau as $x_r \to 0$ remains at constant voltage whereas the plateau at high voltage shifts negative in potential with increasing excess Li, y. Likewise peak Q_2' in dx_r/dV (Fig. 11e) remains centred on nearly the same voltage regardless of the excess Li amount whereas Q_1' is shifted negatively. Regardless of the x scale that is considered (Fig. 11c and f), both entropy profile peaks, S_1' and S_2', shift negatively with changing y. Fig. 11f shows a systematic trend in the suppression of S_1' and S_2'. As shown in eqn (24), this scale, rather than one in Fig. 11c, relates to the experimentally accessible ΔS. Although the slope of the curve, dΔS/dx_r, is independent of the defect concentration for voltages $V > 4.15$ V, there is a lateral separation in the curves. This separation, shown also in the right hand side of Fig. 11d–e, arises from different net Li–Li interactions resulting from the different number of pinned sites. These interactions become identical in the Li filled lattices so the left hand sides of each profile tend to the same value.

Open Access Article. Published on 25 July 2018. Downloaded on 6/18/2025 4:30:21 AM.
This article is licensed under a Creative Commons Attribution 3.0 Unported Licence.

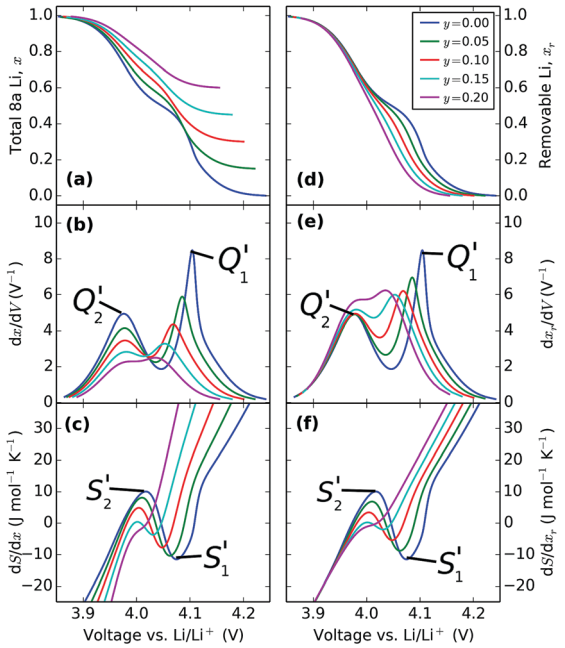

Fig. 11 Effect of varying the excess Li amount, y, with the same interaction parameters in the model: ε_0 = 4.10 eV, J_1 = 30 meV, J_2 = −1.25 meV and δ = 1.25 meV.

3.5 Relating simulated and experimental results

We directly compare simulated and experimental voltage (Fig. 12a–c), dx_r/dV (Fig. 12d–f) and entropy profiles (Fig. 12g–i). Three scenarios are considered: in model 1 (M1), the interaction parameters which optimally fitted the profiles for $Li_xMn_2O_4$ by the method described in Section 2.5 were assumed to remain constant with respect to the excess Li amount, y, in the same way as the results presented in Fig. 11d–f. The observed changes then resulted only from the effect of pinned Li. In model 2 (M2), profiles were individually optimised for each y value, and all interaction parameters were allowed to vary. For clarity, the shift in the entropy change scale due to the vibrational entropy parameter, ΔS_{vib} was omitted from the lines M1 and M2 in Fig. 12g–i. Consequently, these two curves are vertically shifted from the experimental data points, since the only effect of the ΔS_{vib} parameter is to cause a vertical shift in the entropy change scale. Model 2b (M2b) is identical to M2 except that the contribution from ΔS_{vib} is included in the former curve. All experimental profiles were normalised with respect to the actual capacity of the second discharge cycle, and hence we consider our model with respect to the removable Li content, x_r, similarly to the right hand column of Fig. 11.

A comparison of the results from M1 with the experimental profiles reveals that, while the pinned Li effect partly explains the reduced amplitudes in dx_r/dV and system entropy values with increasing y, the model suggests that the intercalation potential window narrows more than is actually observed. Furthermore, the upper voltage plateau shifts negatively with increasing y, which is not reflected in the experimental data. Consistently with our previous Monte Carlo study of point defects in $Li_xMn_2O_4$,[37] the pinned Li sites in the model cause an excessive suppression of the amplitude of the entropy profile peaks. There, only one pinned Li site per defect was assumed,

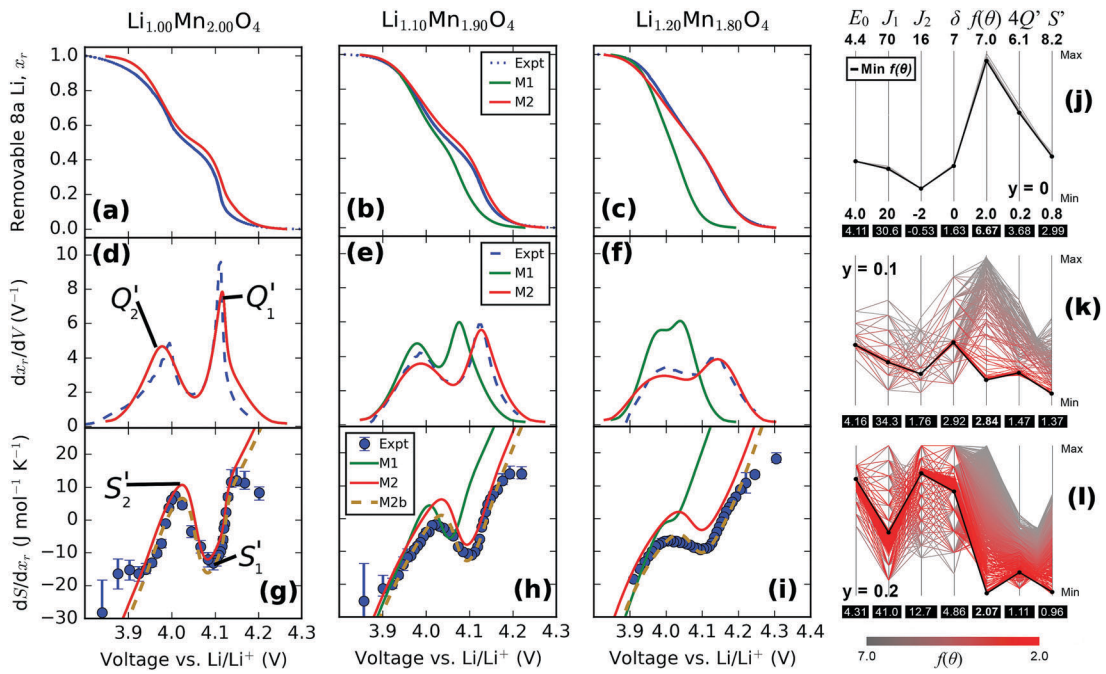

Fig. 12 Comparison of experimental ("Expt") and simulated data ("M1", "M2" and "M2b"). Cathode composition is indicated along the top row. (a–c) Voltage profiles obtained from the second discharge cycle. (d–f) dx_r/dV profiles, (g–i): entropy profiles. Simulated curves according to model 1 ("M1"), model 2 ("M2") and model 2b ("M2b") are described in the main text. Right hand column: (j–l) visualisation of optimisation procedure using the parallel coordinates method. Defect concentration, y, is indicated beside each respective plot.

This journal is © the Owner Societies 2018

Open Access Article. Published on 25 July 2018. Downloaded on 6/18/2025 4:30:21 AM.
This article is licensed under a Creative Commons Attribution 3.0 Unported Licence.

resulting in quantitative differences between the model and experimental results at 30% defect concentration. Here, with 3 times as many pinned Li sites, the discrepancy can be seen at 10% and 20% defect concentration, as shown in Fig. 12h and i.

Table 5 shows the optimised interaction parameters within the assumptions of model 2b (M2b). There is a trend towards increasing repulsion in both the nearest and second nearest neighbour interactions, J_1 and J_2, as the Li excess, y, increases. However, changes in the interaction across the intercalation range must be taken into account to explain the changes observed in the dQ/dV peaks. For J_2, the (net) interaction switches from being attractive for $y = 0$, to weakly repulsive for $y = 0.10$, to repulsive for $y = 0.20$. There is also a trend towards a higher point term ε_0 as y increases, indicating increasing Li–lattice attraction. The observed trends are consistent with the experimentally determined decrease in the lattice constant as a function of y. The reduced nearest neighbour distance would be expected to lead to an increase in Coulombic repulsion between positively charged Li ions in the lattice. We do not have an explanation for the increase in the δ term with y but it could result from changes in the Coulombic screening across the intercalation range in combination the changing oxidation state of the surrounding Mn ions.

In terms of the numerical values from fitting the simulations to experiments, the optimised values of ε_0 and J_1 determined for the stoichiometric compound, 4.11 eV and 30.7 meV respectively, are very close to those reported in the literature. Kim and Pyun reported 4.12 eV and 37.5 meV by fitting galvanostatic intermittent titration technique (GITT) curves using Monte Carlo methods[29] while Gao *et al.* reported 4.145 eV and 37.5 meV using mean field methods.[34] The negative sign of J_2 determined in the present work is consistent with these works but the magnitude, $|J_2| = 0.5$ meV, is somewhat lower. Gao *et al.* determined $J_2 = -5$ meV[34] while Kim and Pyun reported $J_2 = -4$ meV.[29] The discrepancy likely results from the extra degree of freedom and physical insight allowed by the δ parameter; it can be seen from Fig. 9 that the reported values of J_2 would result in dQ/dV peaks much sharper and narrower than the experimental ones. It is not possible to compare the values determined as a function of y since prior work assumed that the interaction parameters did not vary as a function of the defect concentration.[34,46,64]

The effect of the fitting process itself on the determined parameters can also be considered, as shown in Fig. 12j–l. This method is known as ''parallel coordinates'' and is described elsewhere.[65,66] All input parameters in the optimisation procedure and a map to the resulting values of the objective function ($f(\theta)$) from the fitting procedure are shown. For clarity, the values of ΔS_{vib} were omitted from Fig. 12j–l as the convergence of the optimisation procedure was found to be insensitive to this parameter. To produce these plots, all data from the brute force method and the simplex procedure were aggregated together. The values of the fit to the individual curves, dQ/dV and entropy profiles, are denoted here as $4Q'$ and S', respectively. A more comprehensive presentation of the fitting to all the experimental results is shown in the ESI,† Fig. S2.

Fig. 12j and k show that, for $y = 0$ and $y = 0.1$, the minimum $4Q'$ and S' values almost exactly coincide with the weighted fit to both curves, $f(\theta)$. However, with increasing amounts of excess Li, most clearly shown at $y = 0.2$ in Fig. 12l, quantitative differences between the fits to the two curves arise. The figure shows that the total objective value, $f(\theta)$ is almost exactly coincident with the value of S', while the overall optimum value for dQ/dV, denoted by $4Q'$, is linked to a different set of input energy parameters than the global optimum. However, the qualitative interpretation of increasing Li–Li repulsion is unaffected by fitting individually to dQ/dV or entropy profile curves, or a weighted sum of both curves, as shown in the ESI,† Fig. S2.

In general, Fig. 12j and k indicate increasing complexity in determining the overall optimum $f(\theta)$ as the excess Li amount, y, increases. The reason is that the peak widths and amplitudes of dQ/dV and entropy profiles become broader and weaker, respectively, as y increases. Consequently, there is less available information to determine the optimal parameter set. For example, for $y = 0.2$, a decrease in J_1 can be compensated for by an increase in J_2 with a minimal change in the fit quality. This observation has important implications for modelling voltage and entropy profiles in commercial cathodes with mean field methods because these electrodes are designed to intentionally suppress order/disorder transitions, *i.e.* peak amplitudes are reduced.

It is also likely that the assumption of the Bragg–Williams approximation that there are no correlations between the sublattice occupancies (*i.e.* that $\langle n_1 n_2 \rangle = \langle n_1 \rangle \langle n_2 \rangle$), becomes weaker as more pinned Li sites are present in the system. Therefore, we plan to validate these parameters further by performing Monte Carlo simulations using effective cluster interactions determined by density functional theory (DFT) calculations. Based on the work presented here, these simulations will account for changes in the lateral interaction parameters dependent on the lattice parameter. The simulations will determine the point terms in the near neighbourhood of the defects, therefore allowing for local clustering in the orbit of the defects, which could not be captured by the present model. However, the real value of the comparison between the experimental and simulated results is that the method allows for high throughput determination of the trends in the parameters, providing physical insight into the origins of the changes in the peaks.

Table 5 Parameters obtained from the numerical optimisation procedure under the assumptions of model 2b (M2b)

y	ε_0 (eV)	J_1 (meV)	J_2 (meV)	δ (meV)	ΔS_{vib} (kJ mol^{-1} K^{-1})
0	4.11	30.6	−0.5	1.6	−3.5
0.05	4.13	33.8	−0.8	1.7	−3.8
0.1	4.16	34.3	1.8	2.9	−5.0
0.15	4.22	34.6	6.3	4.3	−6.7
0.2	4.32	41.0	12.7	4.9	−7.0

4 Conclusions

We investigated the effect of excess Li, y ($0 \leq y \leq 0.2$) in $Li_{1+y}Mn_{2-y}O_4$ on entropy, voltage and dQ/dV profiles.

Open Access Article. Published on 25 July 2018. Downloaded on 6/18/2025 4:30:21 AM.
This article is licensed under a Creative Commons Attribution 3.0 Unported Licence.

Through numerical optimisation, we compared the results from a mean-field model with experimental entropy and dQ/dV results.

From this work the following insights can be drawn:

(1) Entropy profiles revealed a systematic suppression of the order/disorder transition in the Li/vacancy structure as a function of the amount of excess Li, y, in the lattice.

(2) For all compositions, dQ/dV showed two peaks of unequal magnitudes and shapes. In accordance with previous work, these peaks were also suppressed by excess Li.

(3) Both profiles were modelled through mean-field simulations. An inherent problem in conventional models based on pairwise interactions is profile symmetry either side of $x = 0.5$, contrary to the experimental profiles. To model the observed peak asymmetry, simulations included a single correction term which allowed the interaction parameters to vary linearly over the intercalation range.

(4) Fitting both profiles through numerical optimisation revealed that pinned Li sites, proportional to the defect fraction $x_{pin} = 3y$, resulted in an overestimation of the peak magnitude suppression if the interaction parameters were assumed to be unaffected by the defect concentration, y.

(5) The optimised interaction parameters indicated increased Li–Li repulsion and increased Li–lattice attraction (point term) with increasing excess Li, y.

(6) The same trend was obtained when separately optimising simulated fits to dQ/dV and entropy profiles, or when fitting a weighted sum of both profiles. Quantitative differences between the parameter values from individually optimised fits suggest limitations in the mean-field approximation for high excess Li spinels.

The work provides insight into the physical origins of the peaks in electrochemical and thermodynamic profiles of Li-ion cells, which could lead to a better understanding of the changes observed in aged cells. We highlight the importance of accounting for interaction parameter changes during intercalation, possibly resulting from elastic contributions or charge transfer (changes in oxidation state) during Li (de)insertion. Furthermore, numerical optimisation revealed challenges in fitting the profiles of electrodes in which order/disorder transitions have been intentionally suppressed, as in commercial cathodes. This suggests that the mean-field approximation, widely adopted in the battery community because of its high throughput, requires additional refinement to fully capture the physical processes during intercalation. Therefore, we plan to compare the results of mean-field simulations with Monte Carlo simulations parameterised by effective cluster interactions from DFT calculations, including effects arising from changes in the lattice during Li (de)insertion.

Conflicts of interest

There are no conflicts to declare.

Acknowledgements

We are grateful to the STFC Batteries Network for a Proof of Concept Award (grant number: ST/N002385/1) and the Faraday Institution (faraday.ac.uk; EP/S003053/1), grant number FIRG003, for funding. MPM thanks Denis Kramer from the University of Southampton for his feedback on the mean field approach. MPM thanks Jamie Fairbrother from the Lancaster University Management School for discussions regarding the numerical optimisation approach.

References

1 M. S. Whittingham, *Chem. Rev.*, 2004, **104**, 4271–4301.
2 M. M. Thackeray, *Prog. Solid State Chem.*, 1997, **25**, 1–71.
3 J. B. Goodenough and Y. Kim, *Chem. Mater.*, 2010, **22**, 587–603.
4 M. M. Thackeray, Y. Shao-Horn, A. J. Kahaian, K. D. Kepler, E. Skinner, J. T. Vaughey and S. A. Hackney, *Electrochem. Solid-State Lett.*, 1998, **1**, 7–9.
5 B. Scrosati and J. Garche, *J. Power Sources*, 2010, **195**, 2419–2430.
6 J. Vetter, P. Novák, M. Wagner, C. Veit, K.-C. Möller, J. Besenhard, M. Winter, M. Wohlfahrt-Mehrens, C. Vogler and A. Hammouche, *J. Power Sources*, 2005, **147**, 269–281.
7 X. Han, M. Ouyang, L. Lu, J. Li, Y. Zheng and Z. Li, *J. Power Sources*, 2014, **251**, 38–54.
8 L. Zhou, M. Leskes, T. Liu and C. P. Grey, *Angew. Chem., Int. Ed.*, 2015, **54**, 14782–14786.
9 B. Wu, V. Yufit, Y. Merla, R. F. Martinez-Botas, N. P. Brandon and G. J. Offer, *J. Power Sources*, 2015, **273**, 495–501.
10 K. Maher and R. Yazami, *Electrochim. Acta*, 2013, **101**, 71–78.
11 X.-F. Zhang, Y. Zhao, Y. Patel, T. Zhang, W.-M. Liu, M. Chen, G. J. Offer and Y. Yan, *Phys. Chem. Chem. Phys.*, 2017, **19**, 9833–9842.
12 A. H. Thompson, *Physica B+C*, 1981, **105**, 461–465.
13 J.-S. Kim, J. Prakash and J. R. Selman, *Electrochem. Solid-State Lett.*, 2001, **4**, A141–A144.
14 S. Al Hallaj, R. Venkatachalapathy, J. Prakash and J. R. Selman, *J. Electrochem. Soc.*, 2000, **147**, 2432–2436.
15 Y. Reynier, R. Yazami and B. Fultz, *J. Power Sources*, 2003, **119-121**, 850–855.
16 Y. F. Reynier, R. Yazami and B. Fultz, *J. Electrochem. Soc.*, 2004, **151**, A422–A426.
17 Y. Reynier, J. Graetz, T. Swan-Wood, P. Rez, R. Yazami and B. Fultz, *Phys. Rev. B: Condens. Matter Mater. Phys.*, 2004, **70**, 174304.
18 N. S. Hudak, L. E. Davis and G. Nagasubramanian, *J. Electrochem. Soc.*, 2015, **162**, A315–A321.
19 K. E. Thomas and J. Newman, *J. Power Sources*, 2003, **119-121**, 844–849.
20 K. E. Thomas, C. Bogatu and J. Newman, *J. Electrochem. Soc.*, 2001, **148**, A570.
21 R. Yazami, Y. Reynier and B. Fultz, *ECS Trans.*, 2006, **1**, 87–96.
22 S. Bach, J. P. Pereira-Ramos, N. Baffier and R. Messina, *Electrochim. Acta*, 1992, **37**, 1301–1305.
23 S. Al Hallaj, R. Venkatachalapathy, J. Prakash and J. R. Selman, *J. Electrochem. Soc.*, 2000, **147**, 2432–2436.

Open Access Article. Published on 25 July 2018. Downloaded on 6/18/2025 4:30:21 AM.
This article is licensed under a Creative Commons Attribution 3.0 Unported Licence.

24 T. Kashiwagi, M. Nakayama, K. Watanabe, M. Wakihara, Y. Kobayashi and H. Miyashiro, *J. Phys. Chem. B*, 2006, **110**, 4998–5004.
25 Y. Kobayashi, Y. Mita, S. Seki, Y. Ohno, H. Miyashiro, M. Nakayama and M. Wakihara, *J. Electrochem. Soc.*, 2008, **155**, A14–A19.
26 P. J. Osswald, M. Del Rosario, J. Garche, A. Jossen and H. E. Hoster, *Electrochim. Acta*, 2015, **177**, 270–276.
27 K. Kai, Y. Kobayashi, H. Miyashiro, G. Oyama, S.-I. Nishimura, M. Okubo and A. Yamada, *ChemPhysChem*, 2014, **15**, 2156–2161.
28 S. J. Bazinski and X. Wang, *J. Electrochem. Soc.*, 2014, **161**, A168–A175.
29 S.-W. Kim and S.-I. Pyun, *Electrochim. Acta*, 2001, **46**, 987–997.
30 E. M. Perassi and E. P. M. Leiva, *Electrochem. Commun.*, 2016, **65**, 48–52.
31 E. P. M. Leiva, E. Perassi and D. Barraco, *J. Electrochem. Soc.*, 2017, **164**, A6154–A6157.
32 M. Otero, A. Sigal, E. Perassi, D. Barraco and E. Leiva, *Electrochim. Acta*, 2017, **245**, 569–574.
33 K. Maher and R. Yazami, *J. Power Sources*, 2014, **247**, 527–533.
34 Y. Gao, J. N. Reimers and J. R. Dahn, *Phys. Rev. B: Condens. Matter Mater. Phys.*, 1996, **54**, 3878–3883.
35 R. J. Gummow, *J. Electrochem. Soc.*, 1994, **141**, 1178–1182.
36 A. Van Der Ven, C. Marianetti, D. Morgan and G. Ceder, *Solid State Ionics*, 2000, **135**, 21–32.
37 M. P. Mercer, S. Finnigan, D. Kramer, D. Richards and H. E. Hoster, *Electrochim. Acta*, 2017, **241**, 141–152.
38 B. Ammundsen, G. R. Burns, M. S. Islam, H. Kanoh and J. Roziere, *J. Phys. Chem. B*, 1999, **103**, 5175–5180.
39 A. R. Natarajan, J. C. Thomas, B. Puchala and A. Van der Ven, *Phys. Rev. B*, 2017, **96**, 134204.
40 V. L. Chevrier, S. P. Ong, R. Armiento, M. K. Y. Chan and G. Ceder, *Phys. Rev. B: Condens. Matter Mater. Phys.*, 2010, **82**, 075122.
41 M. Verbrugge, D. Baker, B. Koch, X. Xiao and W. Gu, *J. Electrochem. Soc.*, 2017, **164**, E3243–E3253.
42 C. R. Birkl, E. McTurk, M. R. Roberts, P. G. Bruce and D. A. Howey, *J. Electrochem. Soc.*, 2015, **162**, A2271–A2280.
43 C. R. Birkl, M. R. Roberts, E. McTurk, P. G. Bruce and D. A. Howey, *J. Power Sources*, 2017, **341**, 373–386.
44 T. Ohzuku and A. Ueda, *J. Electrochem. Soc.*, 1997, **144**, 2780–2785.
45 H. Berg, J. O. Thomas, W. Liu and G. C. Farrington, A neutron diffraction study of Ni substituted $LiMn_2O_4$, *Solid State Ionics*, 1998, **112**, 165–168.
46 R. Darling and J. Newman, *J. Electrochem. Soc.*, 1999, **146**, 3765–3772.
47 G. Ceder and A. Van Der Ven, *Electrochim. Acta*, 1999, **45**, 131–150.
48 W. Liu, K. Kowal and C. G. Farrington, *J. Electrochem. Soc.*, 1998, **145**, 459–465.
49 J. A. Nelder and R. Mead, *Comput. J.*, 1965, **7**, 308–313.
50 Y. Gao and J. R. Dahn, *J. Electrochem. Soc.*, 1996, **143**, 1783–1788.
51 M. Wang and A. Navrotsky, *J. Solid State Chem.*, 2005, **178**, 1182–1189.
52 J. Cho, *J. Mater. Chem.*, 2008, **18**, 2257–2261.
53 A. Yamada, *J. Solid State Chem.*, 1996, **122**, 160–165.
54 X. Hao, X. Lin, W. Lu and B. M. Bartlett, *ACS Appl. Mater. Interfaces*, 2014, **6**, 10849–10857.
55 C. P. Grey and N. Dupré, *Chem. Rev.*, 2004, **104**, 4493–4512.
56 Y. J. Lee and C. P. Grey, *J. Electrochem. Soc.*, 2002, **149**, A103–A114.
57 K. Thomas and J. Newman, *J. Power Sources*, 2003, **119**, 844–849.
58 V. I. Kalikmanov and S. W. De Leeuw, *Solid State Ionics*, 2002, **154-155**, 195–201.
59 E. V. Vakarin, J. P. Badiali, M. D. Levi and D. Aurbach, *Phys. Rev. B: Condens. Matter Mater. Phys.*, 2000, **63**, 014304.
60 E. V. Vakarin and J. P. Badiali, *J. Phys. Chem. B*, 2002, **106**, 7721–7724.
61 T. Ohzuku, M. Kitagawa and T. Hitai, *J. Electrochem. Soc.*, 1990, **137**, 40–46.
62 X. Q. Yang, X. Sun, S. J. Lee, J. McBreen, S. Mukerjee, M. L. Daroux and X. K. Xing, *Electrochem. Solid-State Lett.*, 1999, **2**, 157–160.
63 M. R. Palacín, G. G. Amatucci, M. Anne and Y. Chabre, *J. Power Sources*, 1999, **81-82**, 627–631.
64 T. Kudo and M. Hibino, *Electrochim. Acta*, 1998, **43**, 781–789.
65 J. Heinrich and D. Weiskopf, Eurographics 2013 – State of the Art Reports, 2013.
66 M. D'Ocagne, *Coordonnées parallèles et axiales: méthode de transformation géométrique et procédé nouveau de calcul graphique déduits de la considération des coordonnées parallèles*, Gauthier-Villars, Paris, 1885.